Thermo X https://doi.org/10.70401/tx.2026.0037

Supplementary information

Raman thermometry indicates aggregation-induced localized hotspots in optical tweezers

Hongkai Zhang, Nan Zhang, Xiaona Huang, Yunsong Pang, Shijing Wu, Dezhao Huang, Yanan Yue

Supplementary Information for

Raman Thermometry Reveals Aggregation-induced Localized Hotspots in Optical Tweezers

This Supplementary Information file includes:

Notes S1 to S10

Figures S1 to S6

Table S1

Note S1. Optical force model for the PS microsphere

The 5 μm PS microsphere lies outside the Rayleigh regime and was treated with a vector-spherical-wave calculation following the T-matrix framework of Nieminen et al. [1]. For a homogeneous isotropic sphere, this treatment is equivalent to generalized Lorenz-Mie theory. The incident and scattered fields are expanded in vector spherical wave functions, and the optical force is obtained from the momentum-flux change evaluated with the Maxwell stress tensor.

$$F = \oint \langle T \rangle \cdot n \, dS \tag{S1}$$

For comparison with optical-tweezers literature, the radial force is written using the dimensionless radial force efficiency Q_r. This normalization separates the optical power from the electrodynamic calculation:

$$F_r = \frac{n_m P Q_r}{c} \tag{S2}$$

where F_r is the radial force, n_m is the refractive index of the surrounding water, P is the optical power at the sample, c is the speed of light, and Q_r is calculated from the T-matrix/GLMT solution. Because the response is linear in the optical field intensity, F_r scales linearly with P for a fixed optical geometry and particle position.

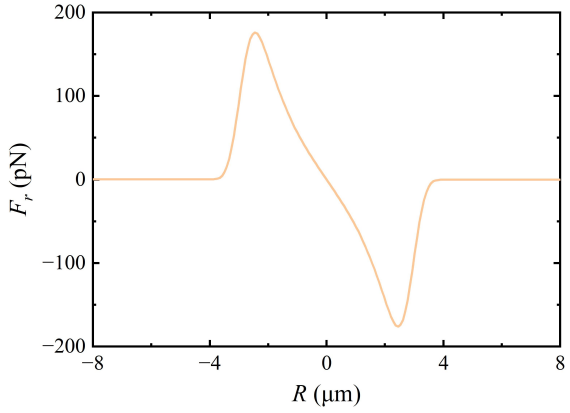


Figure S1. Radial optical force on a 5 μm PS microsphere calculated using the vector-spherical-wave T-matrix method. The force changes sign at the beam axis and reaches a maximum restoring magnitude of approximately 176 pN. Parameters: vacuum wavelength 1064 nm, NA = 0.50, water refractive index 1.33, PS refractive index 1.5694, and P = 0.100 W.

The calculation used λ_0 = 1064 nm, n_m = 1.33, n_{PS} = 1.5694, a = 2.5 μm, NA = 0.50, circular polarization, and P = 0.100 W. The sphere was translated radially through the focal plane while its axial coordinate was fixed. A stable radial equilibrium is obtained when $F_r = 0$ at the beam axis. **Figure S1** shows an antisymmetric radial force about the beam axis. The force vanishes at r = 0 and satisfies $rF_r < 0$ on either side, confirming a restoring equilibrium. The quartz interface, spherical aberration, axial offset, and hydrodynamic coupling are not included, so the calculated force is used to establish trapping feasibility rather than as a direct experimental calibration.

Note S2. Rayleigh force and polarizability of Au nanoparticle

For a 60 nm-diameter Au NP, the size parameter in water is $2\pi n_m a/\lambda_0 \approx 0.236$. The Rayleigh approximation then gives a first estimate of the radial gradient force [2].

$$x = \frac{2\pi n_m a}{\lambda_0} \tag{S3}$$

The complex dipole polarizability of a sphere embedded in water is

$$\alpha = 4\pi\varepsilon_0\varepsilon_m a^3 \frac{\varepsilon_p - \varepsilon_m}{\varepsilon_p + 2\varepsilon_m} \tag{S4}$$

where $\varepsilon_m = n_m^2$, a = 30 nm, and ε_p is the relative permittivity of Au. We used ε_p = -41+ i3.5 at 1064 nm. For a Gaussian beam, I(r) is the radial intensity distribution and the radial gradient force is

$$F_r = \frac{2\pi n_m a^3}{c} Re\left[\frac{\varepsilon_p - \varepsilon_m}{\varepsilon_p + 2\varepsilon_m}\right] \frac{\partial I}{\partial r} \tag{S5}$$

$$I(r) = I_0 exp\left(\frac{-2r^2}{{w_0}^2}\right) \tag{S6}$$

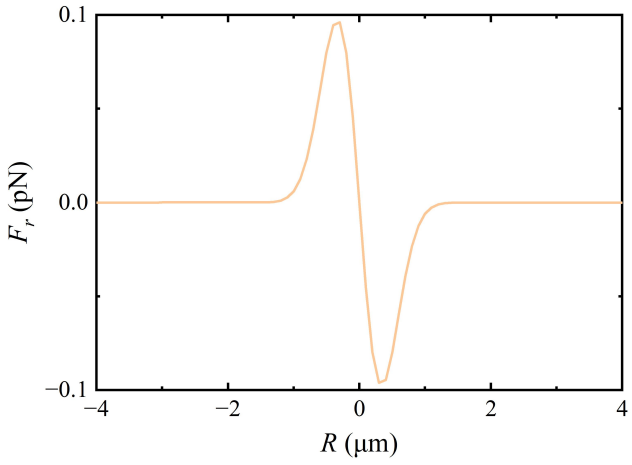


Figure S2. Radial gradient force on a 60 nm Au nanoparticle in the 1064 nm Gaussian beam. The force is restoring on both sides of the beam axis and reaches a maximum magnitude of approximately 0.096 pN. Parameters: particle radius 30 nm, Au relative permittivity -41+i3.5, water refractive index 1.33, Gaussian waist 0.677 μm, and P = 0.100 W.

As shown in **Fig. S2**, the Rayleigh force is much smaller than the force on the PS microsphere but biases Au nanoparticles towards the high-intensity region. This estimate includes only the radial gradient force; scattering, particle-particle interactions, thermophoresis, and near-wall flow are not included.

Note S3. Raman thermometry and uncertainty propagation

Over the calibration range, the fitted peak position was modeled as a linear function of temperature:

$$\omega(T) = \omega_{ref} + \chi(T - T_{ref}) \quad \text{(S7)}$$

where $\chi = d\omega/dT = -0.0054\ cm^{-1}\ K^{-1}$. For a measured shift $\Delta\omega = \omega - \omega_{ref}$, the temperature rise relative to the reference condition is

$$\Delta T = \frac{\Delta\omega}{\chi} \quad \text{(S8)}$$

Here, ω_{ref} is the pre-bubble baseline for the same composition; absolute reporter temperatures add ΔT to the ambient reference temperature. When the peak position is fitted as a function of trapping power, $\Delta\omega = \beta P + b$, the temperature-power coefficient is

$$S_T = \frac{dT}{dP} = \frac{\beta}{\chi} \quad \text{(S9)}$$

If the uncertainties in β and χ are independent, first-order propagation gives

$$\sigma_{ST} = |\beta/\chi|\ [(\sigma_\beta/\beta)^2 + (\sigma_\chi/\chi)^2]^{(1/2)} \quad \text{(S10)}$$

In the main analysis, the temperature–power uncertainties were obtained by dividing the Raman-shift–power regression uncertainty by the calibrated coefficient magnitude. Table S1 summarizes the regression quantities used in this conversion. If $\sigma\chi$ from the calibration fit is included, all temperature–power uncertainties should be enlarged according to Eq. S10.

Table S1. Regression quantities used to convert Raman-shift slopes into PS-reported temperature-power coefficients.

Au stock-dispersion fraction	Raman-shift slope ($cm^{-1}\ W^{-1}$)	Temperature-power coefficient ($K\ W^{-1}$)	Interpretation
0 vol.%	−0.29 ± 0.06	53.5 ± 10.9	Background heating in the trap
0.3 vol.%	−0.60 ± 0.13	110.4 ± 23.8	Intermediate reporter response
1 vol.%	−0.93 ± 0.10	170.3 ± 18.2	Strongest pre-bubble reporter response

Note S4. Heating produced by the 532 nm Raman probe

The Raman probe power was 8.36 mW and the measured spot diameter was approximately 60 μm. Linear interpolation of the Hale–Querry data gives a water absorption coefficient $\alpha_{532} = 3.56 \times 10^{-2}$ m^{-1} at 532 nm [3]. For a Gaussian beam radius w = 30 μm, an effective radial heat-sinking distance R = 2.5 mm, and water thermal conductivity $k_w = 0.60$ W m^{-1} K^{-1}, the steady line-source estimate is

$$\Delta T_{532} \approx \frac{\alpha_{532} P_{532}}{2\pi k_w} ln(\frac{R}{w}) \quad \text{(S11)}$$

Substitution gives $\Delta T_{532} = 3.50 \times 10^{-4}$ K, which is below 1 mK and negligible compared with the temperature rises measured while varying the 1064 nm trapping power. The estimate includes water absorption only. Any fixed direct absorption by PS at 532 nm would be common to all trapping-power conditions and cannot account for the observed power-dependent Raman shift.

Note S5. Raman spectra in different media

The PS ring-breathing band near 1000 cm^{-1} was used as the temperature calibration. **Figure S3** compares spectra measured in air and water at the same room temperature and fitted with the same Voigt function. The peak positions were 1000.28 ± 0.02 cm^{-1} in air and 1000.27 ± 0.02 cm^{-1} in water. This control experiment demonstrates that the influence of the medium on the Raman shift of PS is minimal.

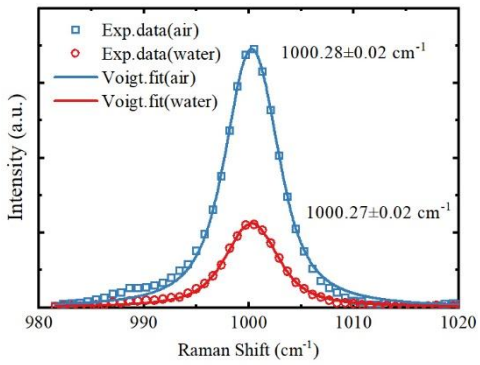


Figure S3. Comparison of the PS ring-breathing Raman band measured in air and water at the same room temperature. Symbols represent the experimental data, and solid lines represent the corresponding Voigt fits.

Note S6. Comparison of particle accumulation and bubble formation in Au-NP and PS dispersions

To determine whether the observed bubble formation originates from Au nanoparticles or simply from particle accumulation in the optical trapping region, we performed control experiments using pure Au-NP and pure PS dispersions under the same experimental conditions. **Figures S4(a)** and **S4(b)** show side-view dark-field images of the Au-NP dispersion. At the beginning of

the observation, only weak and relatively dispersed scattering is visible in the irradiated region. With continued laser irradiation, the scattering signal becomes more localized and pronounced, indicating the accumulation of Au nanoparticles within the observation region. The accumulation process was also examined from the top view. The Au nanoparticles are initially relatively dispersed, as shown in **Fig. S4(c)**. After continued irradiation, a localized particle-rich region develops, as displayed in **Fig. S4(d)**. **Figure S4(e)** shows that a bubble subsequently appears in the same region. The side- and top-view observations therefore consistently show that Au-NP accumulation occurs before bubble formation. For comparison, the same experiment was performed using a pure PS dispersion. As shown in **Fig. S4(f)**, PS particles also accumulate markedly within the trapping region. However, no bubble was observed. The clear difference between the pure Au-NP and pure PS dispersions supports the conclusion that the bubble is induced by the Au nanoparticles. This observation is consistent with the role of Au nanoparticles as the primary optical absorbers and heat sources in the present system.

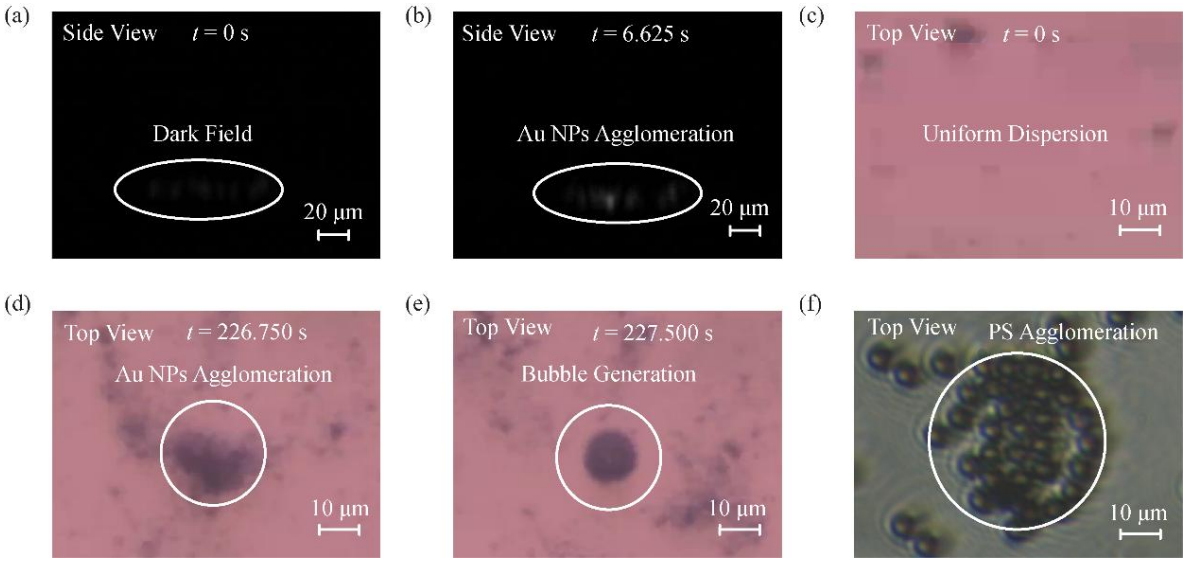


Figure S4. Comparison of particle accumulation and bubble formation in pure Au-NP and pure PS dispersions. (a,b) Side-view dark-field images of the Au-NP dispersion at (t=0) and 6.625 s, respectively, showing progressive Au-NP accumulation. (c–e) Top-view images of the Au-NP dispersion showing the initially dispersed state at (t=0), localized particle accumulation at (t=226.750) s, and subsequent bubble formation at (t=227.500) s. (f) Top-view image of the pure PS dispersion.

Note S7. Comparative electromagnetic-loss analysis of representative Au nanoparticle aggregates

To provide the details of the comparative electromagnetic calculation described in the main text, two-dimensional finite-element models were constructed using the electromagnetic waves, frequency-domain (EWFD) interface. The model contained a 5 μm PS particle and 60 nm Au nanoparticles in water. Four representative Au configurations were considered: an isolated particle, an x-aligned dimer, a compact trimer, and a compact seven-particle cluster. For the

aggregated configurations, neighboring Au particles were modeled as touching (g = 0 nm). All geometries were centered at the same Gaussian beam waist so that the calculated differences arose from particle number and interparticle electromagnetic coupling rather than from changes in illumination position.

The incident field was an x-polarized Gaussian beam with a wavelength of λ_0 = 1064 nm and a focusing radius of w_0 = 0.677 μm. A unit-amplitude background field was used for all configurations. Accordingly, these calculations provide a normalized comparison of geometry-dependent electromagnetic absorption and were not scaled to the experimental laser power. The local optical absorption was characterized by the cycle-averaged electromagnetic power dissipation density, Q_h, with units of W m^{-3}. In the frequency-domain formulation, it is written as

$$Q_h = \frac{1}{2}\mathrm{Re}(\mathbf{J} \cdot \mathbf{E}^*) \tag{S12}$$

where J is the induced current density and E^* is the complex conjugate of the electric field. For each Au configuration containing N particles, Q_h was integrated over all Au domains:

$$Q_N = \iint_{A_{\mathrm{Au},N}} Q_h \, \mathrm{d}A \tag{S13}$$

Because the model is two-dimensional, Q_N has units of W m^{-1}. To remove the trivial increase in total electromagnetic loss caused by the increased number of Au particles, the integrated loss was normalized by the particle number and then by the isolated-particle value:

$$\eta_N = \frac{Q_N}{NQ_1} \tag{S14}$$

where Q_1 is the integrated electromagnetic loss of one isolated Au nanoparticle under the same illumination. The calculated η_N values were 1.00, 7.51, 9.66, and 15.35 for the isolated particle, dimer, trimer, and compact seven-particle cluster, respectively. Because the integrated loss has already been normalized by N, values greater than 1 cannot be explained simply by adding more independent absorbers. Instead, they indicate an enhancement of the average electromagnetic loss per Au particle in the idealized touching aggregates, consistent with interparticle electromagnetic coupling. **Figure S5** shows the spatial distributions of the electromagnetic power dissipation density for the dimer, trimer, and compact seven-particle cluster. The loss becomes increasingly localized within the Au aggregate as the aggregation state increases, in agreement with the normalized integrated-loss values above. These results provide a mechanistic comparison showing that close Au nanoparticle aggregation can substantially enhance local optical absorption.

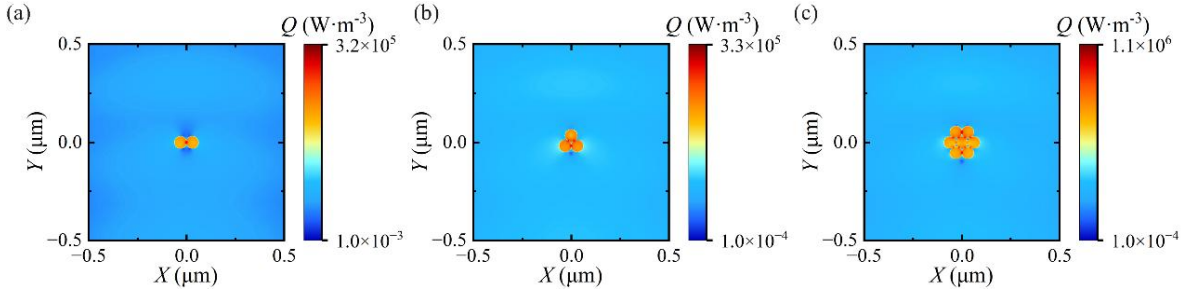


Figure S5. Comparative electromagnetic power dissipation in representative Au nanoparticle aggregates. Spatial distributions of the cycle-averaged electromagnetic power dissipation density for idealized touching Au nanoparticle configurations under identical unit-amplitude, 1064 nm, x-polarized Gaussian illumination: (a) dimer, (b) trimer, and (c) compact seven-particle cluster. Each Au nanoparticle has a diameter of 60 nm and the interparticle gap is g = 0 nm.

Note S8. Bubble formation and reproducibility for the 1 vol.% Au condition

The 1 vol.% Au condition was selected for bubble-formation analysis because its stronger photothermal response allowed bubble nucleation to be reached within the available laser-power range. Before nucleation, the PS Raman shift showed an approximately linear dependence on trapping power, allowing the pre-bubble temperature–power relation to be extrapolated toward the bubble-onset condition. In contrast, no bubble was observed for the 0.3 vol.% Au dispersion within the experimentally accessible power range. At 0.337 W, bubble formation was observed in three independent experiments for the 1 vol.% Au dispersion, as shown in **Figure S6**, confirming the reproducibility of the bubble event under this condition.

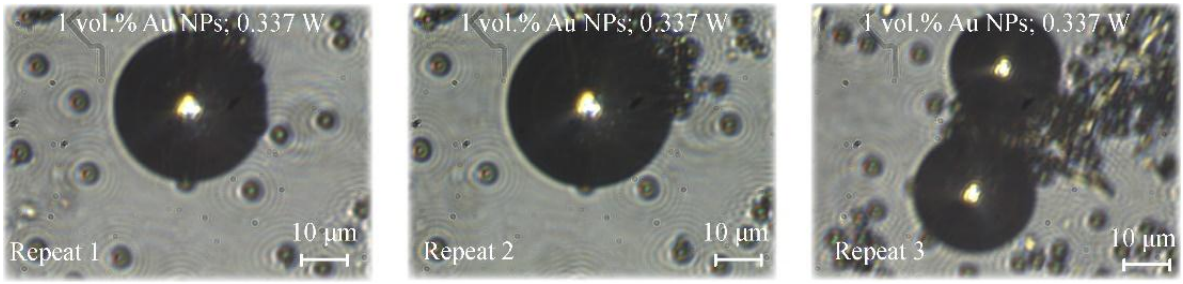


Figure S6. Reproducibility of bubble formation in the 1 vol.% Au dispersion. Three independent bubble-formation experiments performed at a trapping power of 0.337 W. A localized bubble is observed in each measurement, confirming the reproducibility of bubble formation under this condition.

Note S9. Calculations of steady temperature field

In the absence of significant convection over the nanoscale hotspot region, the steady temperature field in water is governed by

$$\nabla \cdot (k_w \nabla T) + q_h = 0 \qquad \text{(S15)}$$

For a compact heat source with total absorbed power Q in an infinite medium, the far-field conductive temperature rise scales as

$$\Delta T(r) \approx \frac{Q}{4\pi k_w r} \tag{S16}$$

For a uniformly heated spherical source of radius a_h, the surface temperature rise is approximately

$$\Delta T_s \approx \frac{Q}{4\pi k_w a_h} \tag{S17}$$

Equations S16 and S17 show that localizing the same absorbed power within a smaller region increases the near-field temperature while producing a much smaller rise at a micrometre-scale reporter. This is the heat-transfer origin of the scale separation used in the main text: T_{local} near an Au aggregate can be high even when the PS-reported temperature remains moderate. The Raman signal reports a weighted average over the PS particle and optical sampling volume:

$$T_{Raman} = \frac{\int W(r)T(r)dV}{\int W(r)dV} \tag{S18}$$

The thermal diffusion time over a length L is

$$\tau_{th} \approx \frac{L^2}{\alpha_w} \tag{S19}$$

With $\alpha_w \approx 1.4 \times 10^{-7}$ m^2 s^{-1}, L = 100 nm gives $\tau_{th} \approx 7 \times 10^{-8}$ s. Local thermal equilibration near Au aggregates is much faster than the 90 s Raman integration time, so the stable, pre-bubble Raman shifts can be treated as quasi-steady.

Note S10. Other interpretation of bubble formation below the boiling temperature

At 1 vol.% Au, the mean bubble-onset power was 0.341 ± 0.011 W (n = 3). Extrapolating the pre-bubble PS temperature–power relation gives T ≈ 293 K + (163.810 K W^{-1})(0.341 W) ≈ 351 K from the pre-bubble PS reporter coefficient is below the normal boiling point of water. This value should be interpreted only as a PS-reported temperature extrapolated from the stable linear regime. It is not the local water temperature adjacent to an Au aggregate and is not a direct boiling criterion. The PS-reported temperature, the local water temperature adjacent to an Au aggregate, and the stochastic nucleation threshold for a vapor/gas bubble are different quantities.

$$T_{local}(r_{hotspot}) \geq T_{nuc}$$

$$T_{nuc} = T_{nuc}(\text{surface, gas content, pressure, exposure time}) \tag{S20}$$

The bubble-onset threshold depends on dissolved gas, surface defects, contact-line geometry, local pressure, and heating duration. Nanoparticle aggregates and the quartz-water interface can lower the practical onset threshold relative to homogeneous nucleation in clean water.

References

[1] Nieminen TA, Loke VLY, Stilgoe AB, Knöner G, Branczyk AM, Heckenberg NR, et al. Optical tweezers computational toolbox. Journal of Optics A: Pure and Applied Optics. 2007;9:S196-S203. doi:10.1088/1464-4258/9/8/S12.

[2] Harada Y, Asakura T. Radiation forces on a dielectric sphere in the Rayleigh scattering regime. Optics Communications. 1996;124:529-541. doi:10.1016/0030-4018(95)00753-9.

[3] Hale GM, Querry MR. Optical constants of water in the 200-nm to 200-µm wavelength region. Applied Optics. 1973;12:555-563. doi:10.1364/AO.12.000555.

[4] Govorov AO, Richardson HH. Generating heat with metal nanoparticles. Nano Today. 2007;2:30-38. doi:10.1016/S1748-0132(07)70017-8.

[5] Baffou G, Quidant R. Thermo-plasmonics: using metallic nanostructures as nano-sources of heat. Laser & Photonics Reviews. 2013;7:171-187. doi:10.1002/lpor.201200003.

[6] Baffou G, Polleux J, Rigneault H, Monneret S. Super-heating and micro-bubble generation around plasmonic nanoparticles under continuous-wave illumination. Journal of Physical Chemistry C. 2014;118:4890-4898. doi:10.1021/jp411519k.